Climate Dynamics (2022) 58:3155–3171
https://doi.org/10.1007/s00382-021-06088-x

Impacts of stratospheric polar vortex changes on wintertime precipitation over the northern hemisphere

Jiankai Zhang[1,2] · Huayi Zheng[1] · Mian Xu[1] · Qingqing Yin[1] · Siyi Zhao[1] · Wenshou Tian[1] · Zesu Yang[3]

Received: 16 July 2021 / Accepted: 28 November 2021 / Published online: 9 January 2022

Abstract

The impacts of Arctic stratospheric polar vortex (SPV) on wintertime precipitation over the Northern Hemisphere are analyzed based on various datasets. Two groups of ensemble climate model experiments with the SPV nudged towards strong and weak states are performed to clarify stratospheric impacts on changes in precipitation. During weak SPV events, precipitation rates over the western and southeastern parts of North Pacific Ocean, the southern part of North Atlantic Ocean, and Southern Europe are larger, whereas the total precipitation rates over the central North Pacific, the northern part of North Atlantic and Northern Europe are smaller than those during strong SPV events. The SPV-induced changes in precipitation over the North Atlantic are stronger than those over the North Pacific. The convective (large-scale) precipitation changes play a major role in the total precipitation changes over the southern (northern) parts of middle latitudes associated with SPV changes. The tropospheric zonal wind deceleration around 60°N associated with weak SPV events is responsible for lower-tropospheric anomalous cyclonic flows over the two oceans at middle latitudes. The anomalous cyclonic flows lead to more large-scale precipitation in the southeastern parts of the oceans and less large-scale precipitation over Northern Europe and the central North Pacific during weak SPV events. The stratosphere–troposphere coupling over the North Atlantic is stronger than that over the North Pacific, leading to stronger large-scale precipitation responses over the former region. In addition, convective precipitation rates between 30 and 45°N are basically larger during weak SPV events than during strong SPV events. This is because more baroclinic waves associated with a southward shift of storm tracks during weak SPV events cause more heat exchanges between the lower latitudes and higher latitudes. Consequently, the upper tropospheric temperature and static ability between 30 and 45°N are reduced, leading to larger convective available potential energy and more convective precipitation during weak SPV events.

1 Introduction

The polar vortex, which is characterized by strong circumpolar westerly winds, is one of the most important components of atmospheric circulations in winter. There are two quite different polar vortices in the Arctic regions, i.e., the tropospheric vortex and the stratospheric vortex, which are not directly connected with each other (Waugh 2017). Baldwin and Dunkerton (2001) pointed out that the Northern Annular Mode (NAM) pattern propagates downward from the stratosphere to the troposphere during anomalous polar vortex events, which not only links the stratospheric vortex with the tropospheric vortex, but also suggests that the stratospheric signal may precede the occurrence of tropospheric weather anomalies. Douville (2009) conducted a numerical experiment, in which the polar vortex above the tropopause is nudged towards the vortex state in the real atmosphere, and found that the simulations of Arctic Oscillation and surface climate are significantly improved. This confirms that the SPV changes can influence tropospheric processes and surface climate instead of simply covarying with the troposphere. Furthermore, there are sound evidences that the sudden stratospheric warming corresponding to an extremely weak SPV is often followed by extremely cold weather and heavy snowstorms in the middle latitudes (e.g. Mitchell et al 2013; Vial et al 2013; Overland et al. 2016; Domeisen et al. 2020; Charlton-Perez et al 2021).

✉ Jiankai Zhang
jkzhang@lzu.edu.cn

[1] College of Atmospheric Sciences, Lanzhou University, Lanzhou 730000, China

[2] Southern Marine Science and Engineering Guangdong Laboratory (Zhuhai), Zhuhai 519080, China

[3] School of Atmospheric Sciences, Chengdu University of Information Technology, Chengdu 610225, China

Several mechanisms have been proposed to explain the impacts of SPV on the tropospheric processes, including the downward control principle (Haynes et al. 1991; Song and Robinson 2004), adjustments of the tropospheric flow to stratospheric potential vorticity anomalies (Hartley et al. 1998; Ambaum and Hoskins 2002), downward planetary-wave reflection (Perlwitz and Harnik 2003; Kretschmer et al 2018; Song and Wu 2019) and the modulation of tropospheric waves by the stratospheric flow (Kunz et al 2009; Hu et al 2018; Zhang et al 2020). As the stratospheric winds decelerate, the tropospheric jet stream shifts equatorward due to the wave-mean flow interactions, and the opposite is true for a strengthened SPV (Kidston et al 2015; Lim et al 2016). The position of the tropospheric jet stream is closely related to tropospheric meteorological parameters (e.g. temperature, precipitation and winds, etc.). For instance, when the tropospheric jet shifts equatorward in response to the weakened SPV, cold weather prevails in Northern Europe, eastern United States and Northern Asia (e.g. Kolstad et al. 2010; Tomassini et al. 2012; Sigmond et al. 2013; Li et al. 2017). Tomassini et al. (2012) estimated that approximately 40% of wintertime cold outbreaks over Northern Europe is preceded by weak SPV. On the other hand, the strengthening of SPV can lead to poleward shift of the tropospheric jet, which is related to winter storms and extreme rainfalls in the United Kingdom (Huntingford et al. 2014; Knight et al. 2017). Anomalously strong SPV in winter means a delay in breakup of polar vortex in the subsequent early spring. Wei et al. (2007) revealed that the timing of SPV collapse significantly affects the positions of the Azores High and the Icelandic Low in February, which in turn affects weather and climate in the Atlantic and European regions.

In addition to the impacts of changes in the SPV strength, the SPV position changes may also exert a significant influence on the tropospheric weather and climate. Mitchell et al. (2013) found that the SPV displacement events can cause a 1.5 K cooling in the northeastern part of North American continent. They are also responsible for the increase in the frequency of blocking in Canada, which is not observed during SPV splitting events. Zhang et al. (2016) pointed out that the shift of the SPV towards the Eurasian continent in February over the past four decades could reduce the tropospheric temperature over Eurasia and the northeastern part of North America in late winter and early spring. Furthermore, the heavy snowstorm that struck South China in the winter of 2008 is caused by the development of the Ural blocking and the persistent southward outbreak of cold air from the polar region, which is possibly related to the SPV displacement towards East Asia 2–3 weeks prior to the snowstorm occurrence (Liu et al. 2008; Chen et al. 2011). Although the abovementioned studies have suggested a link between the SPV displacement and tropospheric weather and climate changes in Eurasia and especially in East Asia, the impacts on the troposphere caused by changes in the SPV position are generally weaker than those caused by changes in the SPV strength (Mitchell et al. 2013).

The aforementioned studies mainly focused on the Arctic SPV impacts on tropospheric and surface winds and temperature. In fact, the SPV changes may also influence tropospheric precipitation. Previous studies have reported that the strengthening of Antarctic SPV caused by the Antarctic ozone hole can lead to more precipitation at high latitudes and subtropical regions in the Southern Hemisphere, and less precipitation at middle latitudes during austral summer (Son et al. 2009; Kang et al. 2011; Purich et al. 2012; Bai et al 2016). Some studies pointed out that Arctic SPV changes could also affect the precipitation in the tropics and subtropics (e.g. Xie et al. 2016; Hu et al. 2019), and that in the northern middle latitudes (Ma et al. 2019; Zhang et al. 2019). Ma et al. (2019) found that Arctic stratospheric ozone increase in March corresponding to a weakened SPV can reduce precipitation over the northwestern United States in April. Zhang et al. (2019) found more precipitation in the northwestern North Pacific in late winter and spring during weak SPV events than during strong SPV events. However, the underlying mechanisms responsible for the SPV impacts on precipitation over the Northern Hemisphere remain unclear. This study addresses this issue based on observations and two numerical experiments with SPV nudged towards abnormally strong and weak states respectively. This paper is organized as follows. The data, methods and model are described in Sect. 2. In Sect. 3, the responses of precipitation over the Northern Hemisphere to the SPV changes are presented. In Sects. 4 and 5, the underlying mechanisms responsible for large-scale and convective precipitation anomalies associated with SPV events are analyzed. The results and discussion are presented in Sect. 6.

2 Data, methods and numerical experiments

2.1 Data

The Global Precipitation Climatology Project (GPCP) monthly precipitation data is used in this study. The GPCP product offers a consistent analysis of global precipitation that combines various satellite data sets over land and ocean with a gauge analysis over land. Data from rain gauge stations, satellites, and sounding observations have been merged to estimate monthly rainfall on a 2.5-degree global grid. More details about the GPCP data can be found in Adler et al. (2003). In addition, the meteorological fields (e.g. temperature, horizontal winds, geopotential height, etc.) are extracted from the ERA-Interim reanalysis data

(Dee et al. 2011). The data used here covers the period from 1980 to 2017. We use daily data to calculate moisture flux convergence, eddy momentum flux, eddy heat flux and eddy kinetic energy. Otherwise, we use monthly data to make composite analysis for zonal wind, geopotential height, convective and large-scale precipitation associated with SPV changes.

2.2 Methods

The present study mainly attempts to explore the impacts of changes in SPV strength on precipitation. Composite analysis of weak and strong SPV events based on ERA-Interim reanalysis dataset is conducted. First, the SPV strength index is defined as the December–January–February mean zonal wind, which is area-weighted averaged over 60–90°N and is pressure-weighted averaged in the layer between 50 and 10 hPa. The SPV strength index is then detrended and normalized with respect to the period from 1980 to 2017. Finally, the weak and strong SPV events are identified based on the normalized SPV strength index that is smaller and greater than –1 and + 1 standard deviation, respectively.

Bootstrap resampling test is used to calculate the statistical probability that two sample populations have meaningfully distinct averages. Assume we have two samples, X and Y (sample sizes: N_1 and N_2). Data batches with sample sizes n_1 and n_2 ($n_1 \leq N_1$, $n_2 \leq N_2$) are repeatedly and randomly sampled from the original samples by 1000 times. The statistics including mean and variance of these resamples are then calculated to estimate the true probability distributions. Finally, the upper and lower thresholds of the 90% confidence level are calculated as the 5th and 95th of 1000-time bootstrap resampling. The difference is considered statistically significant when zero is excluded in this confidence level (Gilleland 2020).

In this study, the vertically integrated moisture flux convergence (VIMFC, Darand and Pazhoh 2019) from 1000 to 300 hPa is represented as follows:

$$VIMFC = -\frac{1}{g}\int_{1000hPa}^{300hPa}\left(\frac{\partial uq}{\partial x} + \frac{\partial vq}{\partial y}\right)dp,$$

where q is the specific humidity, u and v are the zonal and meridional wind, respectively, p is the pressure and g is the gravity acceleration.

Convergence of eddy flux of zonal momentum (EMC) is used to diagnose wave feedback process. The EMC is calculated as follows:

$$EMC = -\frac{\partial u'v'}{\partial y} - \frac{\partial u'w'}{\partial z},$$

where prime presents the zonal anomaly from the zonal average. u, v and w denote zonal, meridional and vertical wind velocity, respectively.

Convective available potential energy (CAPE, Doswell and Rasmussen 1994) is used to diagnose impacts of changes in the SPV strength on convective activities. CAPE exists within the conditionally unstable layer of the troposphere, i.e. the free convective layer, where an ascending air parcel is warmer than the ambient air. Any value greater than zero indicates convective instability. In this study, CAPE in the Interim data is directly obtained from https://apps.ecmwf.int/datasets/data/interim-full-daily/levtype=sfc, while the CAPE in the model simulation is calculated by integrating vertically the local buoyancy of a parcel from the level of free convection (LFC) to the equilibrium level (EL):

$$CAPE = \int_{Z_{LFC}}^{Z_{EL}} g\left(\frac{T_{v,air} - T_{v,env}}{T_{v,env}}\right),$$

where Z_{LFC} is the height of the level of free convection and Z_{EL} is the height of the equilibrium level (neutral buoyancy), $T_{v,air}$ is the virtual temperature of the air parcel, $T_{v,env}$ is the virtual temperature of the environment.

The transient eddy kinetic energy (EKE) is calculated to represent the synoptic-scale transient eddy activity (Blackmon 1976; Hoskins and Hodges 2002):

$$EKE = \overline{u'}^2 + \overline{v'}^2,$$

where the prime represents 2–8 days band-pass filtering, and the overbar means temporal average in winter.

2.3 Numerical model and experiment designs

The specific chemistry version of the Whole Atmosphere Community Climate Model version 4.0 (WACCM-SC) is used in the present study. This model is a component of the Community Earth System Model (CESM) version 1.2.0, developed and maintained by the National Center for Atmospheric Research (NCAR). The horizontal resolution of the model is 1.9° × 2.5° and there are 66 vertical levels extending from 1000 hPa to around 0.0006 Pa. More details of the model can be found in Smith et al (2014). The weak and strong SPV ensemble runs are conducted as follows.

First, the control run is performed for 70 years. All the forcings (e.g. aerosol, sea surface temperature, sea ice, stratospheric ozone and etc.) in the control run are all fixed at the climatological state of 1980–2005. The outputs of the control run at each October 1st of the 21 to 70 model years are used as initial files for two ensemble runs, i.e. weak SPV (R1) and strong SPV (R2). Each ensemble run consists of 50 members and each member integrates from October 1st to the subsequent February 28th. For the two ensemble runs, the Arctic SPV (north of 60°N and above 200 hPa) from December 1st to the subsequent February 28th is nudged towards weak and strong states respectively and the nudging efficient is 1. The nudging coefficient between 300 and 200 hPa and 55–60°N increases linearly from 0 to 1 for the purpose to minimize the artificial effect of abrupt change in the coefficient. The method to identify the weak and strong SPV events is described in Sect. 2.2. Composite horizontal wind and temperature fields for the weak and strong SPV events are based on data extracted from the MERRA-2 3-h reanalysis dataset (Gelaro et al. 2017), which are used as the reference meteorological fields for the R1 and R2 ensemble runs, respectively.

Previous studies have indicated that the stratosphere-troposphere coupling is strongest in winter (Kushner and Polvani 2004; Cohen et al. 2007; Davini et al. 2014). Therefore, the present study mainly focuses on the impacts of wintertime changes in the SPV strength on precipitation from December to the subsequent February. Figure 1a and c shows the composite differences in zonal wind and geopotential height derived from reanalysis data between weak and strong SPV events. The differences in zonal wind and geopotential height between CESM runs R1 and R2 are also shown in Fig. 1b and d for comparison. Note that the stratospheric zonal wind during weak SPV events (R1) is smaller than that during strong SPV events (R2) in most time of winter. Correspondingly, the stratospheric geopotential height during weak SPV events (R1) is larger than that during strong SPV events (R2) during winter. The reversal of upper stratospheric anomalies in February may be the result of stratospheric vacillation (Holton and Mass 1976). Note that the simulated differences in zonal wind and geopotential height during winter (December–February), when the nudge technology is applied, are nearly the same as those in the composite results, suggesting that it is appropriate to compare the impacts of SPV changes on tropospheric climate using CESM simulation with those using Interim composite analysis. In addition, the differences in zonal wind and geopotential height both propagate downward from the upper stratosphere to the lower stratosphere and even to the

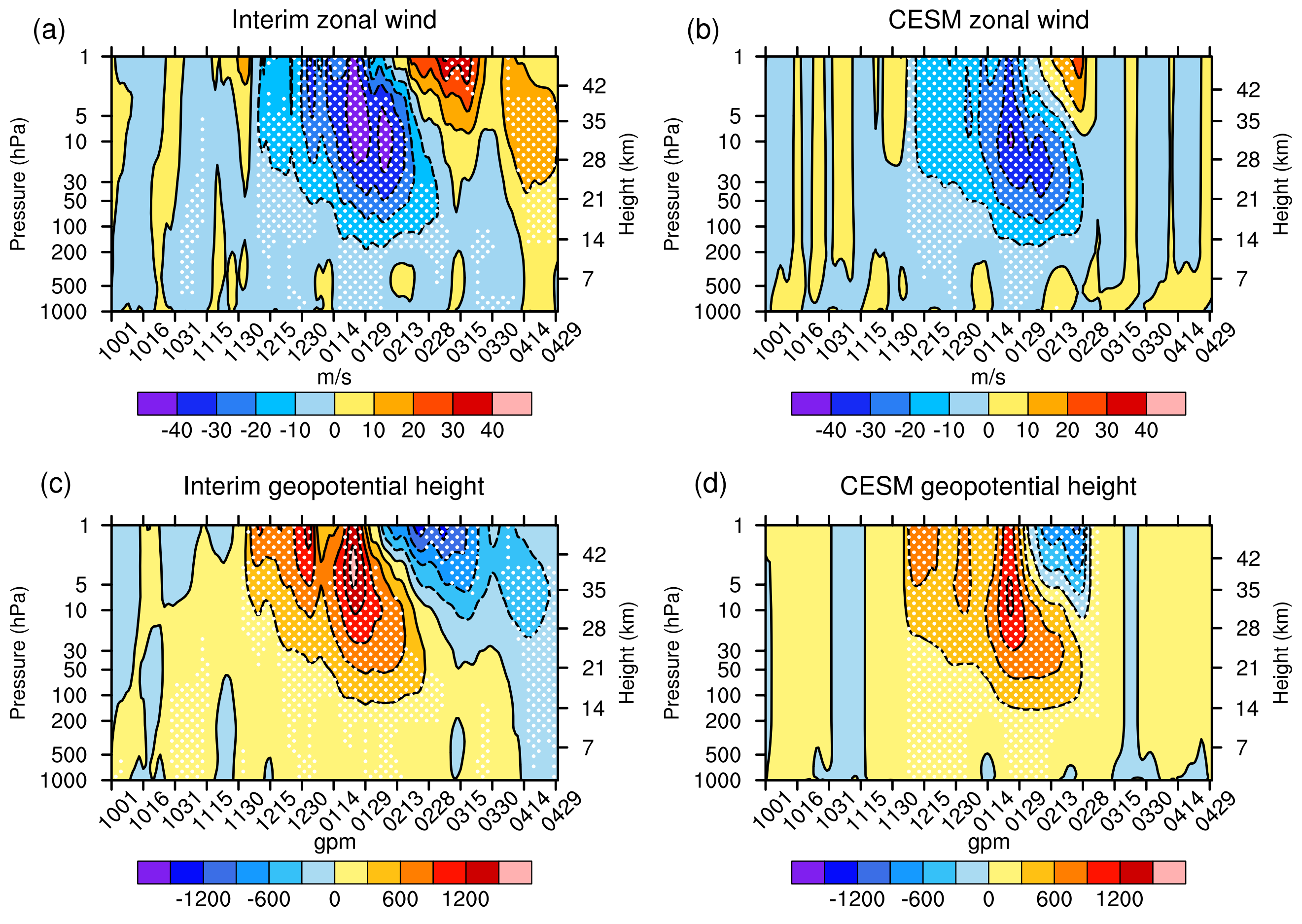

Fig. 1 Time-height cross sections of differences in (**a**) zonal wind (unit: m/s) and (**c**) geopotential height (unit: gpm) derived from Interim reanalysis data between weak and strong SPV events. (**b**) and (**d**) are the same as (**a**) and (**c**), respectively, but for the differences between CESM runs R1 and R2. The differences over the dotted regions are statistically significant at the 90% confidence level according to the bootstrap test

troposphere, which is more significant in CESM simulation than composite results from reanalysis data, implying that the impacts of SPV on the troposphere could be better separated from internal variability using large-ensemble runs (Graf et al. 2014).

3 Responses of precipitation to stratospheric polar vortex changes

Figure 2a and 2b present climatological precipitation rate in winter over the Northern Hemisphere derived from GPCP observations and CESM simulations. Note that the precipitation rates over the Pacific and the Atlantic Oceans are generally larger than those over the continents. In addition, the precipitation rate in the Rockies is also larger than that in most regions of the Northern Hemisphere. The CESM model basically captures the spatial pattern of wintertime precipitation rate displayed in the GPCP observations (Fig. 2b), although the simulated precipitation rate over the Pacific is slightly larger than the observed. The interannual variation of precipitation rate derived from observations is presented in Fig. 2c, which shows larger values over the southern Pacific Ocean, the Rockies and the southern North Atlantic compared to those in other regions of the northern middle latitudes. The spatial distribution and interannual

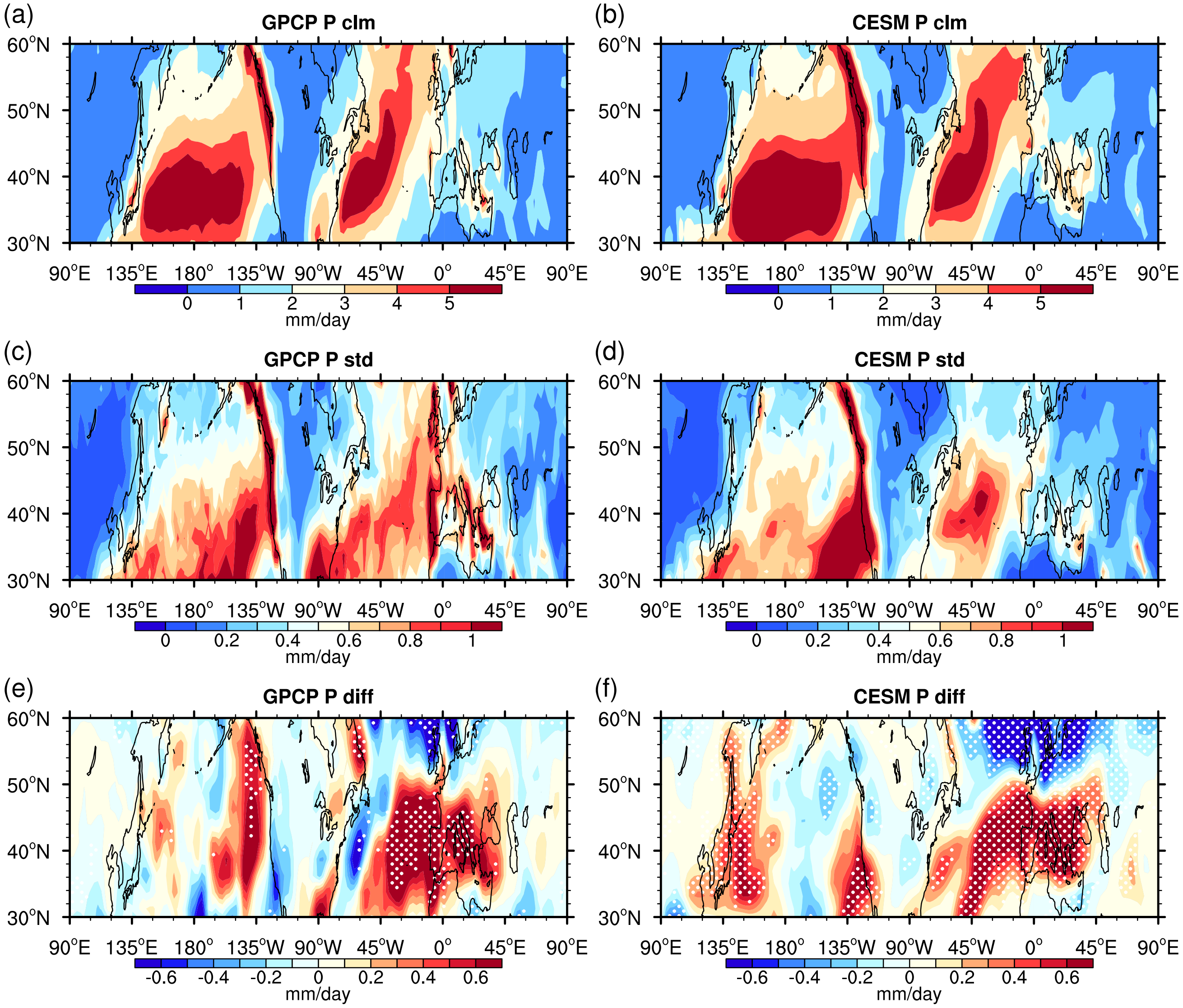

Fig. 2 (**a**) Climatological mean and (**c**) interannual standard deviation of total precipitation rate (unit: mm/day) for the period 1980–2017 based on the GPCP data. (**e**) Differences in total precipitation rate (unit: mm/day) between weak and strong SPV events based on the GPCP data. (**b**) Climatological mean and (**d**) interannual standard deviation of total precipitation rate (unit: mm/day) based on CESM run R1. (**f**) Differences in total precipitation rate (unit: mm/day) between R1 and R2. Dotted regions in (**e**) and (**f**) are for differences statistically significant at the 90% confidence level according to the bootstrap test

variability of precipitation rate are similar between simulations and observations, suggesting that the CESM model can well capture the spatial and temporal features of precipitation over the Northern Hemisphere.

Figure 2e displays the differences in precipitation rate between weak and strong SPV events derived from GPCP data. Precipitation rates over the regions with large interannual variation (e.g. the southeastern North Pacific, the southern parts of the North Atlantic Ocean and Southern Europe) demonstrate noticeable changes associated with anomalous SPV, with more precipitation over these regions during weak SPV events than during strong SPV events. In addition, the regions with small interannual variability (e.g. the northern parts of the North Atlantic Ocean and Northern Europe) also experience significant precipitation changes. Furthermore, the magnitude of the anomalies in precipitation rate related to SPV changes over the North Atlantic Ocean is larger than that over the North Pacific Ocean. Consistent with the results from GPCP data, in CESM simulation, there are more precipitation rates over the western Pacific, southeastern Pacific, southern parts of North Atlantic Ocean and Southern Europe during weak SPV events than those during strong SPV events, while the precipitation rates over the central parts of North Pacific, northern parts of North Atlantic and Northern Europe are reduced during weak WPV events (Fig. 2f). However, the magnitude of increased precipitation rate over the Western Pacific derived from CESM simulation is relatively larger than that derived from GPCP data. In addition, there are less precipitation over the northeastern Pacific during weak SPV events derived from CESM simulation, in contrast to more precipitation over this region derived from GPCP data. It should be pointed out that most of the precipitation anomalies over the North Pacific associated with SPV changes derived from GPCP data are not significant at 95% confidence level, while those are still significant in CESM simulation (not shown), suggesting that the discrepancy in precipitation changes over the North Pacific between GPCP data and CESM simulation may be related to the impacts of internal variability on observation.

The calculation of precipitation rate in the CESM can be divided into two parts, i.e. large-scale (stable) and convective precipitation. The convective precipitation scheme is based on Zhang and McFarlane (1995), while the large-scale precipitation is calculated using prognostic condensate and precipitation parameterization from Zhang et al (2003). In winter, the spatial pattern of climatological mean large-scale precipitation rate is similar to that of total precipitation rate (comparing Fig. 2b and Fig. 3a), although the simulated magnitude of large-scale precipitation is smaller. By contrast, convective precipitation largely occurs over the

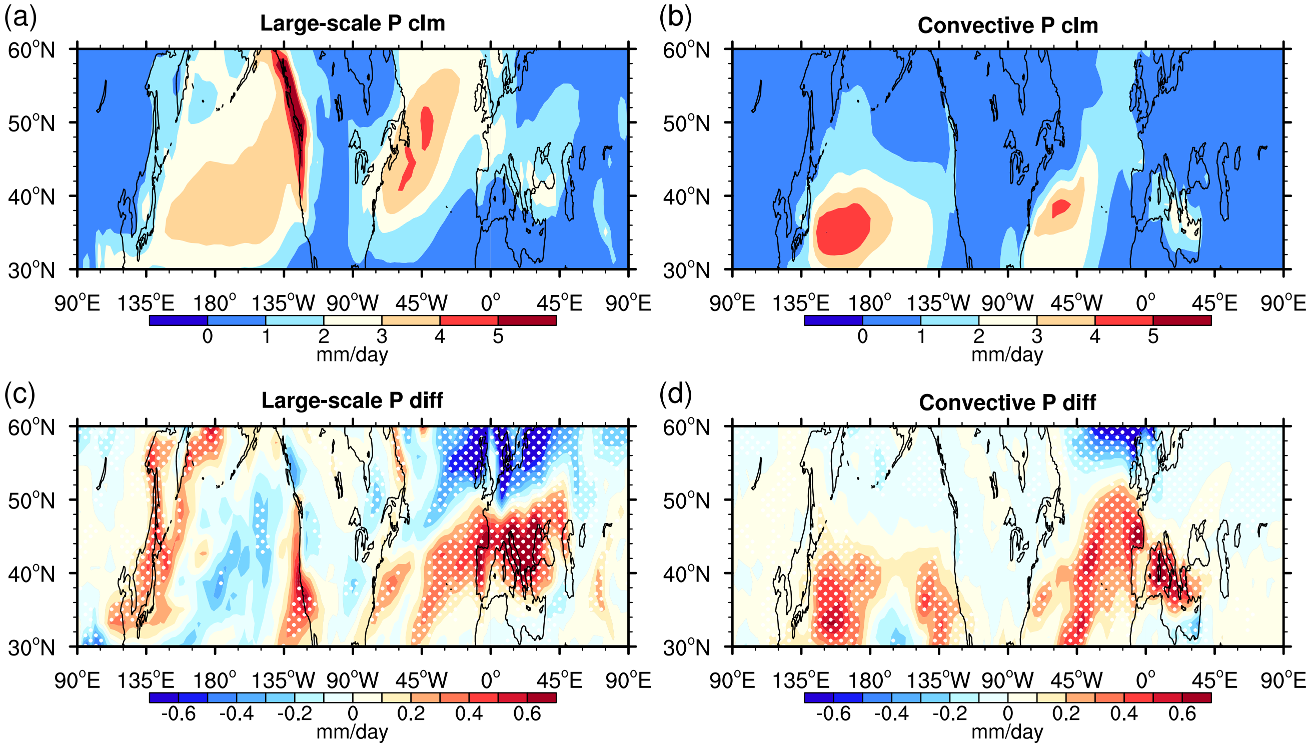

Fig. 3 Climatological mean of (**a**) large-scale and (**b**) convective precipitation rate (unit: mm/day) for CESM R1 experiment. Differences in (**c**) large-scale and (**d**) convective precipitation rate (unit: mm/day) between R1 and R2. The differences over the dotted regions in (**c**) and (**d**) are statistically significant at the 90% confidence level according to the bootstrap test

southern North Pacific and North Atlantic (Fig. 3b) due to more heating over the low-latitude oceans. In the northern parts of North Pacific, the changes in large-scale precipitation rate make dominant contribution to the difference in total precipitation rate between weak and strong SPV events (comparing Fig. 2f and Fig. 3c), while the convective precipitation rate between 30 and 40°N is larger during weak SPV events (Fig. 3d). In the North Atlantic Ocean, both the changes in large-scale and convective precipitation rates have important contributions to the difference in total precipitation rate between weak and strong SPV events (Fig. 3c and d). Table 1 shows the relative contribution of large-scale and convective precipitation to the total precipitation changes over typical regions associated with anomalous SPV events. Overall, the convective precipitation changes contribute more to the total precipitation changes over the southern parts of middle latitudes than large-scale precipitation changes, with the largest contribution over the southwestern North Pacific (77.9%). By contrast, the large-scale precipitation changes play a larger contribution to total precipitation changes over the northern parts of middle latitudes, with the largest contribution in northwestern North Pacific (91.7%). This is understandable since there is more heating in the lower latitudes, favoring the formation of convective precipitation, which accounts for more precipitation changes in the lower latitudes.

4 Mechanisms responsible for large-scale precipitation responses

Generally speaking, large-scale precipitation is closely related to large-scale atmospheric circulation that controls the water vapor transport. Figure 4 shows the differences in geopotential height (color shaded) and zonal wind (contours) at various pressure levels between weak and strong SPV events. In the lower stratosphere (50 hPa), the polar jet decelerates and the geopotential height in the polar region increases during weak SPV events. Meanwhile, zonal winds accelerate at middle latitudes, resembling a NAM-like pattern (Baldwin and Dunkerton 2001). It is also worth noting that the CESM simulated differences in geopotential height and zonal winds (Fig. 4b) are approximately the same as those in the reanalysis data (Fig. 4a), suggesting that the nudged-stratosphere experiments used in this study yield creditable results. In the upper troposphere (300 hPa), the differences in geopotential height and zonal winds are more asymmetric than those at 50 hPa (Fig. 4c, d). In terms of geostrophic equilibrium, negative geopotential height differences between weak and strong SPV events occur to the south of the weakened polar jet. The responses of large-scale circulation to SPV changes are stronger over the North Atlantic than over the North Pacific, which is consistent with larger precipitation responses over the former region. In addition, the simulated responses at 300 hPa are weaker than those in the reanalysis data, particularly over the North Pacific Ocean (Fig. 4d), which may be related to reduced internal variability in the large-ensemble runs. The differences in the lower troposphere (850 hPa) over the North Atlantic Ocean are similar to those at 300 hPa, constituting a barotropic structure. However, the changes in the lower-level circulation over the North Pacific induced by the SPV changes are less significant than those over the North Atlantic Ocean (Fig. 4e and f).

The SPV also has significant impacts on atmospheric circulations in the lower troposphere and even on the surface. As shown in the reanalysis data, compared with the circulations during the strong SPV events, anomalous cyclonic flows occur between 700 and 1000 hPa during weak SPV events, which are accompanied by negative SLP anomalies over the North Pacific and North Atlantic Oceans (Fig. 5a). The simulated lower-tropospheric circulation changes are weaker than those in the reanalysis data (comparing Fig. 5a and Fig. 5b), particularly over the North Pacific Ocean,

Table 1 Relative contributions of large-scale and convective precipitation changes to the total precipitation changes over typical regions

Regions	Percentage contribution of large-scale precipitation (%)	Percentage contribution of convective precipitation (%)
Northern North Atlantic (50–60°N, 45°W–0°)	66.0	34.0
Southern North Atlantic (35–45°N, 45°W–0°)	46.7	53.3
Northern Europe (50–60°N, 0–45°E)	85.1	14.9
Southern Europe (35–42°N, 0–45°E)	42.7	57.3
Southwestern North Pacific (30–45°N, 135°E–180°)	22.1	77.9
Southeastern North Pacific (30–45°N, 150–120°W)	38.2	61.8
Northwestern North Pacific (45–55°N, 135–165°E)	91.7	8.3

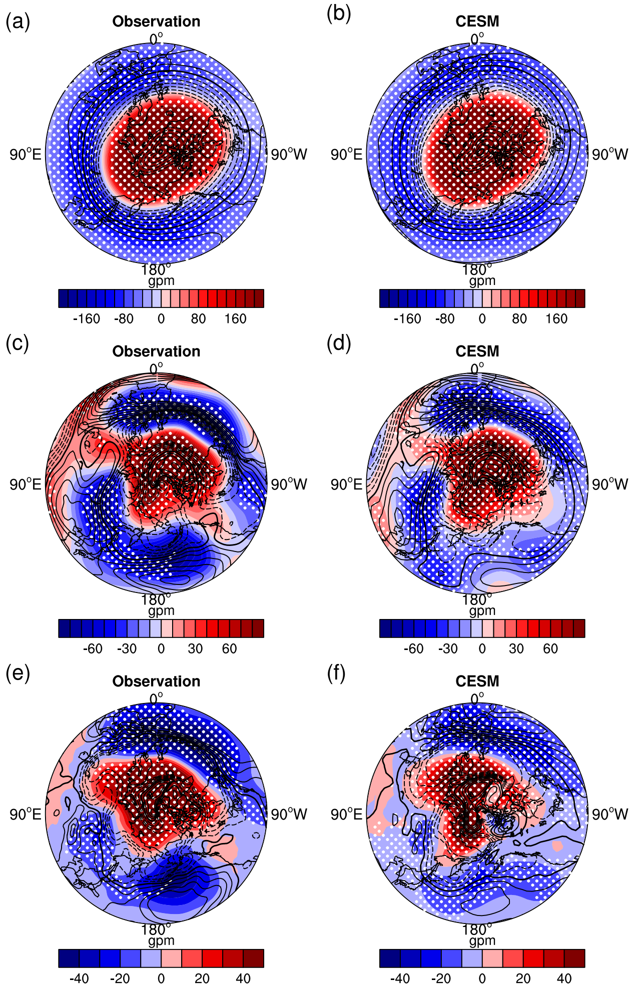

Fig. 4 Differences in geopotential height (color shaded, unit: gpm) and zonal wind (contours, unit: m/s, solid and dashed lines represent positive and negative values, respectively) at (**a**) 50 hPa (contour interval: 2 m/s), (**c**) 300 hPa (contour interval: 1 m/s) and (**e**) 850 hPa (contour interval: 0.5 m/s) between weak and strong SPV events based on the ERA-Interim reanalysis data. (**b**), (**d**), and (**f**) are the same as (**a**), (**c**) and (**e**), respectively, but for the differences between CESM R1 and R2. The differences over the dotted regions are statistically significant at the 90% confidence level according to the bootstrap test

suggesting that the composite anomalies associated with SPV changes include various internal variabilities. Figure 5c and 5d show the differences in moisture flux and its vertically integrated convergence between weak and strong SPV events derived from reanalysis data and CESM simulation. In the reanalysis data, enhanced cyclonic flows are found over the North Pacific (North Atlantic) Ocean, which are accompanied with anomalous southerlies over the eastern Pacific (eastern Atlantic) and northerlies over the central and western Pacific (western Atlantic). This pattern of circulation anomalies leads to large water vapor convergence in the southeastern Pacific and southeastern Atlantic, and precipitation rate is subsequently high over these regions. In contrast, water vapor flux divergence develops over the Northern Europe, leading to less large-scale precipitation there (Fig. 3c, d). In addition, the water vapor flux divergence (convergence) reduces the magnitude of increased (decreased) large-scale precipitation over the southwestern (northwestern) Atlantic during weak SPV events. The anomalous cyclonic flow over the North Pacific is mainly located in the eastern edge, and precipitation decrease largely occurs in the central Pacific based on reanalysis data. However, the precipitation decrease is not noticeable in the simulation. The large precipitation rate over the western Pacific during weak SPV events may be related to anomalous cyclonic flows over the East Asia (Fig. 5a and b). Overall, the magnitude of lower-tropospheric circulation responses over the North Pacific to SPV changes is smaller than that over the North Atlantic, which explains why the magnitude of large-scale precipitation responses over the North Pacific to SPV changes is also smaller (Fig. 2).

The circulation changes over the North Atlantic in response to SPV changes are stronger than those over the North Pacific, which may be attributed to the stronger stratosphere-troposphere coupling over the former region. Figure 6 shows the differences in sub-polar zonal wind over the two oceans between weak and strong SPV events. Given that the latitude (50°N) of the cyclonic flow center over the North Pacific is farther northward than that (40°N) over the North Atlantic by about 10° (Fig. 5), more northward pressure-latitude cross section of wave-mean flow interaction over the North Pacific is shown. In the lower stratosphere (50–150 hPa), zonal winds are weaker to the north of 50°N during weak SPV events than during strong SPV events in both North Pacific and North Atlantic, which indicates that the impacts of SPV changes in the lower stratosphere are zonally symmetric, consistent with results shown in Fig. 4a and 4b. In the troposphere, the area with statistically significant negative zonal wind differences over the North Pacific is smaller than that over the North Atlantic (Fig. 6a, c). In terms of geostrophic balance, cyclonic flows occur in the south of the negative zonal wind differences over both the North Atlantic and the North Pacific, and the former cyclonic flows are stronger (Fig. 5).

Previous studies pointed out that the stratospheric processes affect the tropospheric circulation mainly through wave-mean flow interactions (e.g. Perlwitz and Harnik 2004; Lubis et al 2018; Boljka and Birner 2020; Hu et al 2021). Figure 7 displays the meridional cross sections of the EMC, which is a measure of wave feedback process. Note that, in the North Pacific, large wave flux convergence occurs to the north of 60°*N*, which appears to be anti-phase with zonal wind anomalies over this region (Fig. 6a, b). In the North Atlantic, the tropospheric wave flux convergence occurs more southward than that over the North Pacific (Fig. 7c, d), which is in accord

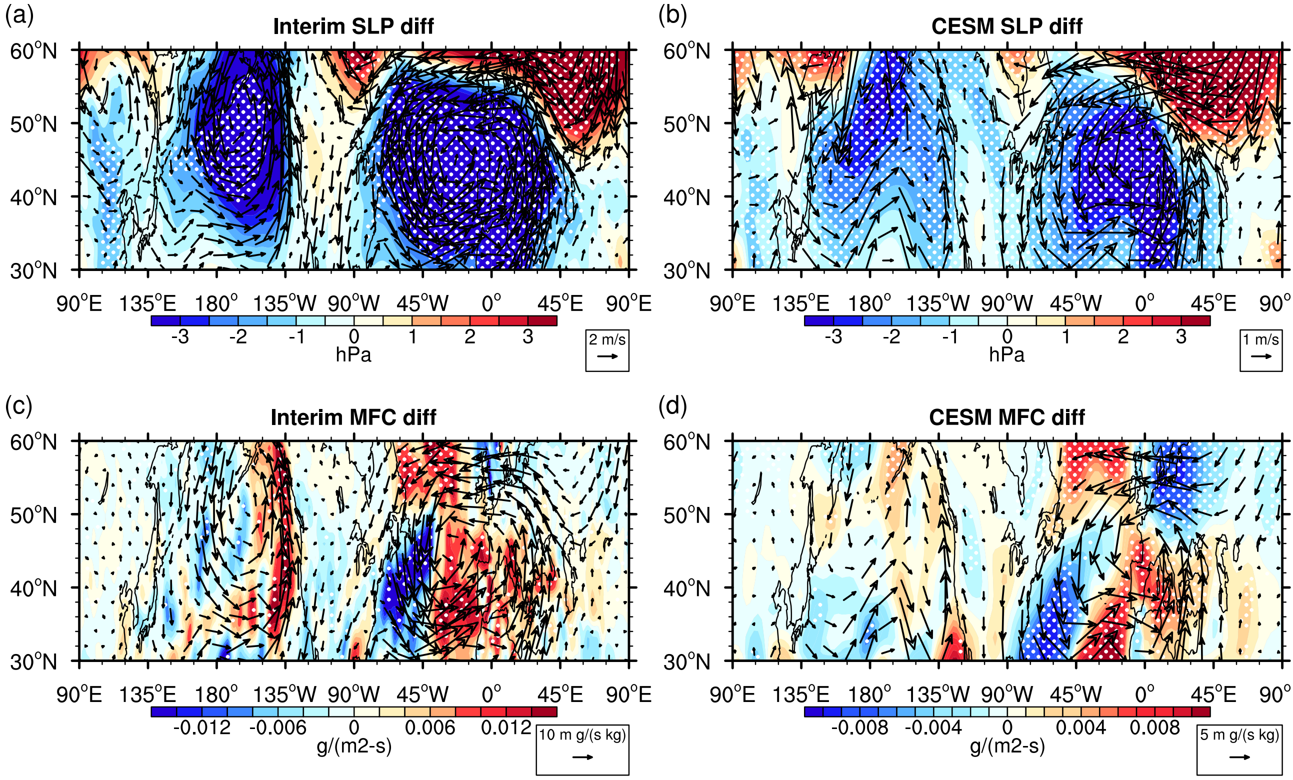

Fig. 5 (**a**) Differences in sea level pressure (color shaded, unit: hPa) and 700–1000 hPa horizontal winds (vectors, unit: m/s) between weak and strong SPV events based on the ERA-Interim reanalysis data. (**c**) Differences in moisture flux convergence vertically integrated from 300 to 1000 hPa [color shaded, unit: g/(m^2 s)] and 700–1000 hPa moisture flux [vectors, unit: m g/(s kg)] between weak and strong SPV events based on the ERA-Interim reanalysis data. (**b**) and (**d**) are the same as (**a**) and (**c**), respectively, but for the differences between CESM R1 and R2. The differences over the dotted regions are statistically significant at the 90% confidence level according to the bootstrap test

with a more southward location of negative zonal wind differences in the troposphere over the North Atlantic (comparing Fig. 6b and Fig. 6d). By contrast, the positive zonal wind differences between WPV and SPV events in the high-latitude troposphere (Fig. 6c, d) over the North Atlantic are related to the enhanced wave flux divergence over this region (Fig. 7c, d). This can be explained by the notion that the convergence (divergence) of eddy momentum flux balances the deceleration (acceleration) of the Coriolis torques forced by anomalous mean meridional circulation (Limpasuvan and Hartmann 2000). It is worth noting that the wave flux feedback processes over the North Atlantic are not only more significant but also more barotropic than those over the North Pacific, which is consistent with the conclusion that the Atlantic jet is primarily eddy driven (e.g. Breiteig 2008; Garfinkel and Hartmann 2011; Li and Wettstein 2012). The more barotropic eddy forcing leads to stronger stratosphere-troposphere coupling over the North Atlantic mentioned above.

5 Mechanisms responsible for convective precipitation responses

According to the above analysis, large-scale precipitation is under strong influences of large-scale horizontal transport of moisture flux. On the other hand, convective precipitation is produced by small-scale convective activities, which can be measured by CAPE. Figure 8 shows the climatological distribution of maximum CAPE and its differences between weak and strong SPV events. Note that the climatological mean CAPE at subtropics is larger than that at higher latitudes (Fig. 8a, b), which is

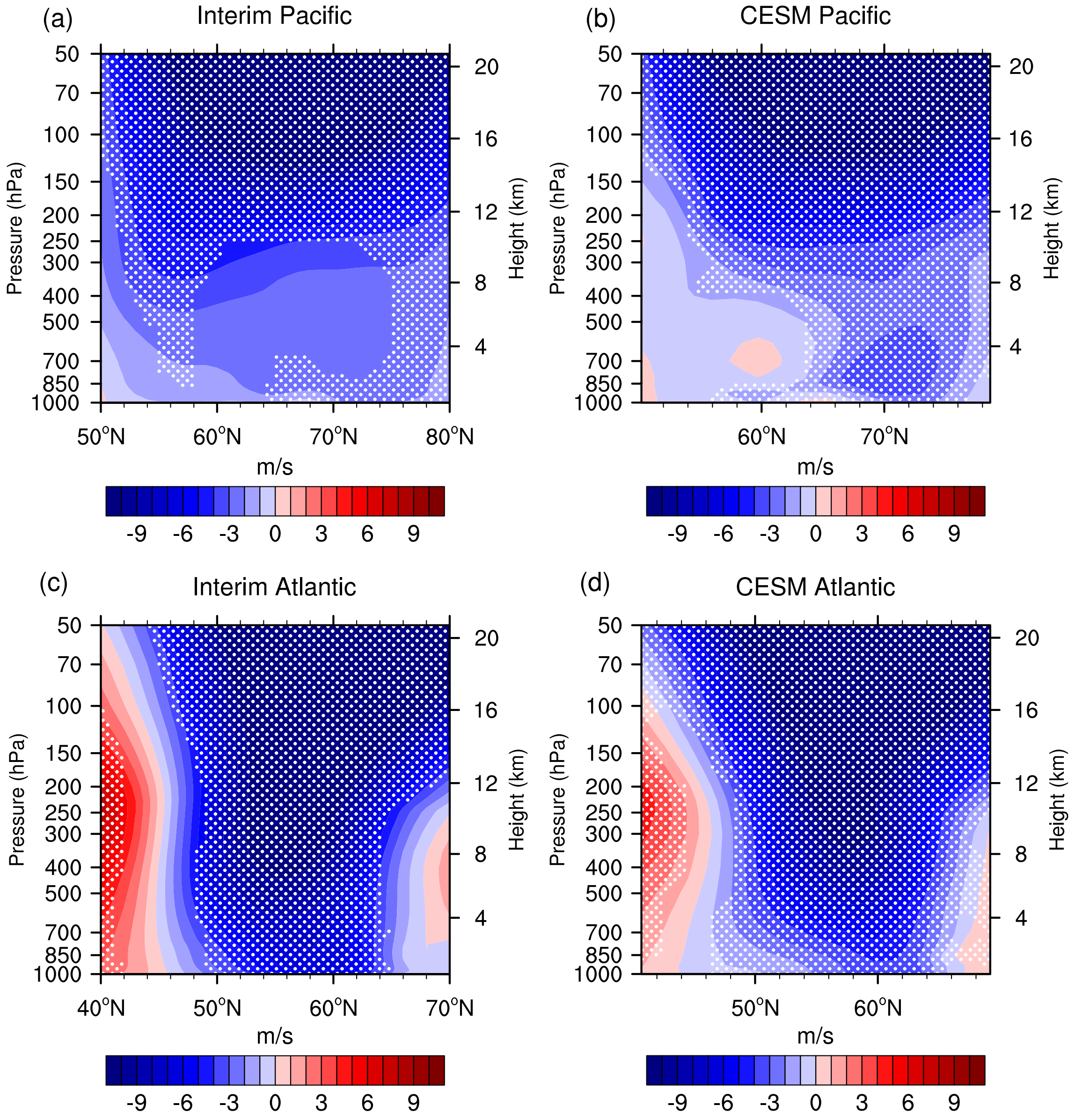

Fig. 6 Pressure-latitude cross sections of differences in zonal wind (color shaded, unit: m/s) between weak and strong SPV events (**a**) along 180° between 50–80°N and (**c**) along 30°W between 40–70°N derived from Interim reanalysis data. (**b**) and (**d**) are the same as (**a**) and (**c**), respectively, but for the differences in zonal wind between CESM R1 and R2. The differences over the dotted regions are statistically significant at the 90% confidence level according to the bootstrap test

understandable due to more radiative heating in the lower latitudes. Furthermore, the CAPEs to the south of 45°N are basically larger during weak SPV events than during strong SPV events (Fig. 8c, d). Particularly, note that larger CAPEs in the southern parts of North Pacific and North Atlantic Oceans as well as the Mediterranean are collocated with larger convective precipitation rates over these regions during weak SPV events than during strong SPV events (Fig. 3d), which supports the notion that the SPV changes can affect convective precipitation through modulating CAPE.

The enhanced CAPE to the south of 45°N associated with weak SPV events is attributed to more unstable airmass over this latitudinal zone. Figure 9 shows the climatological mean and differences in EKE between weak and strong SPV events. Storm tracks are generally identified with the maxima of the EKE (Mbengue and Schneider 2017). Figure 9a and b show clearly that the storm tracks at middle latitudes tilt southwestward. The center of the storm track over

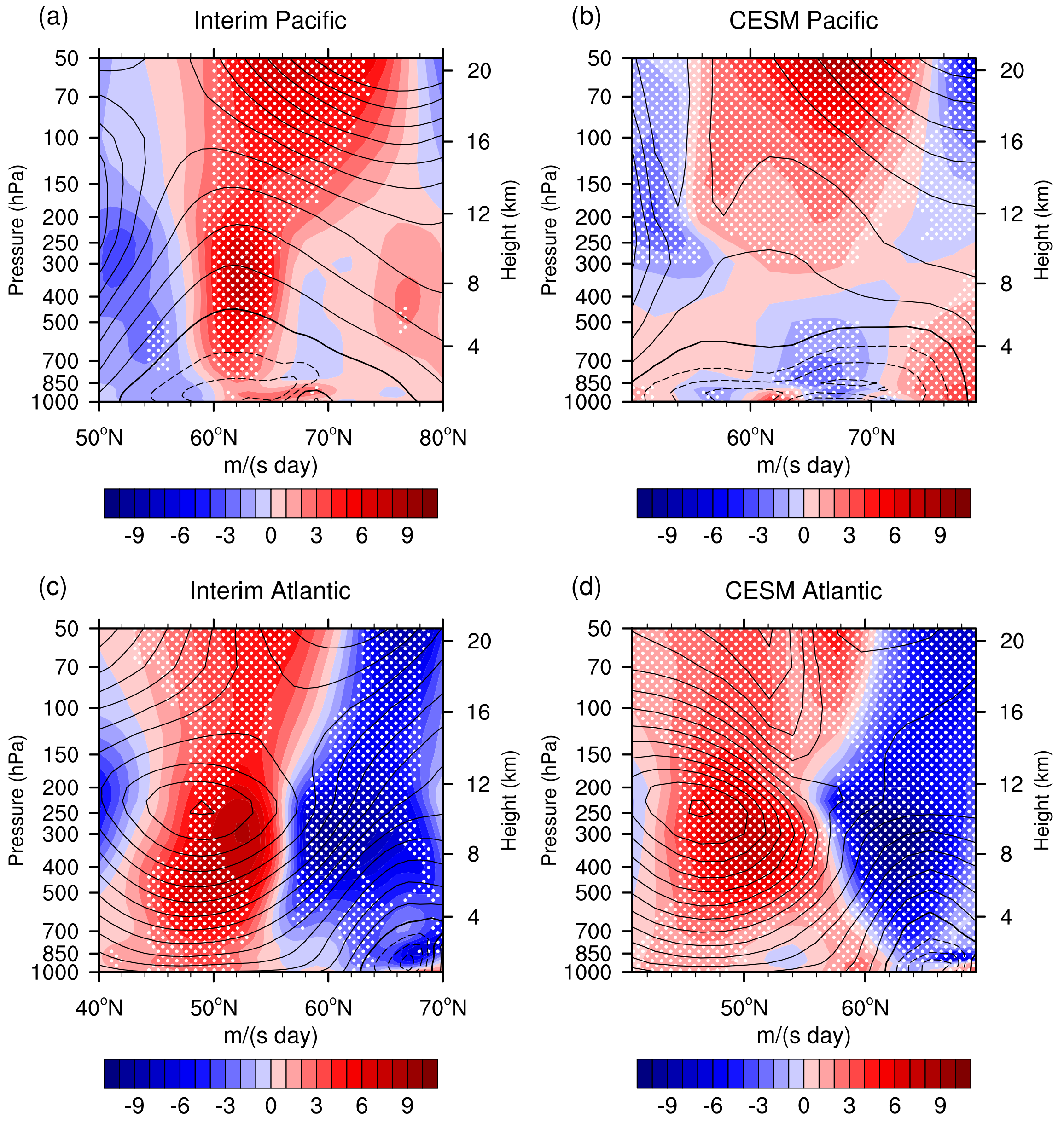

Fig. 7 Pressure-latitude cross sections of differences in EMC [color shaded, unit: m/(s day)] between weak and strong SPV events and climatological mean of zonal winds (contours, unit: m/s, contour interval: 2 m/s, solid and dashed lines represent positive and negative values, respectively) for the period 1980–2017 (**a**) along 180° between 50 and 80°N and (**c**) along 30°W between 40 and 70°N derived from Interim reanalysis data. (**b**) and (**d**) are the same as (**a**) and (**c**), respectively, but for the differences in EMC between CESM R1 and R2 and climatological mean of zonal wind from R1. The differences over the dotted regions are statistically significant at the 90% confidence level according to the bootstrap test

the North Pacific is located around 40°N, while the center over the North Atlantic is at 50°N. As the SPV weakens, the storm tracks over the North Pacific and North Atlantic both shift equatorward, with larger (smaller) EKE in the southern (northern) parts of North Pacific and North Atlantic Oceans during weak SPV events than during strong SPV events. Mbengue and Schneider (2017) proposed that the equatorward shifts of storm tracks or maxima of EKE are corresponding to less convective static stability and thus more convections in the lower latitudes. Larger EKE corresponds to a more unstable atmosphere and more baroclinic waves. Figure 10a and b shows that there are larger northward eddy heat fluxes in the poleward flank of the subtropical jet during weak SPV events than during strong SPV events, which is true in both reanalysis data and CESM simulation. This suggests that more heat is transported from the lower latitudes to the higher latitudes during weak SPV events and this feature is more evident in the upper troposphere between

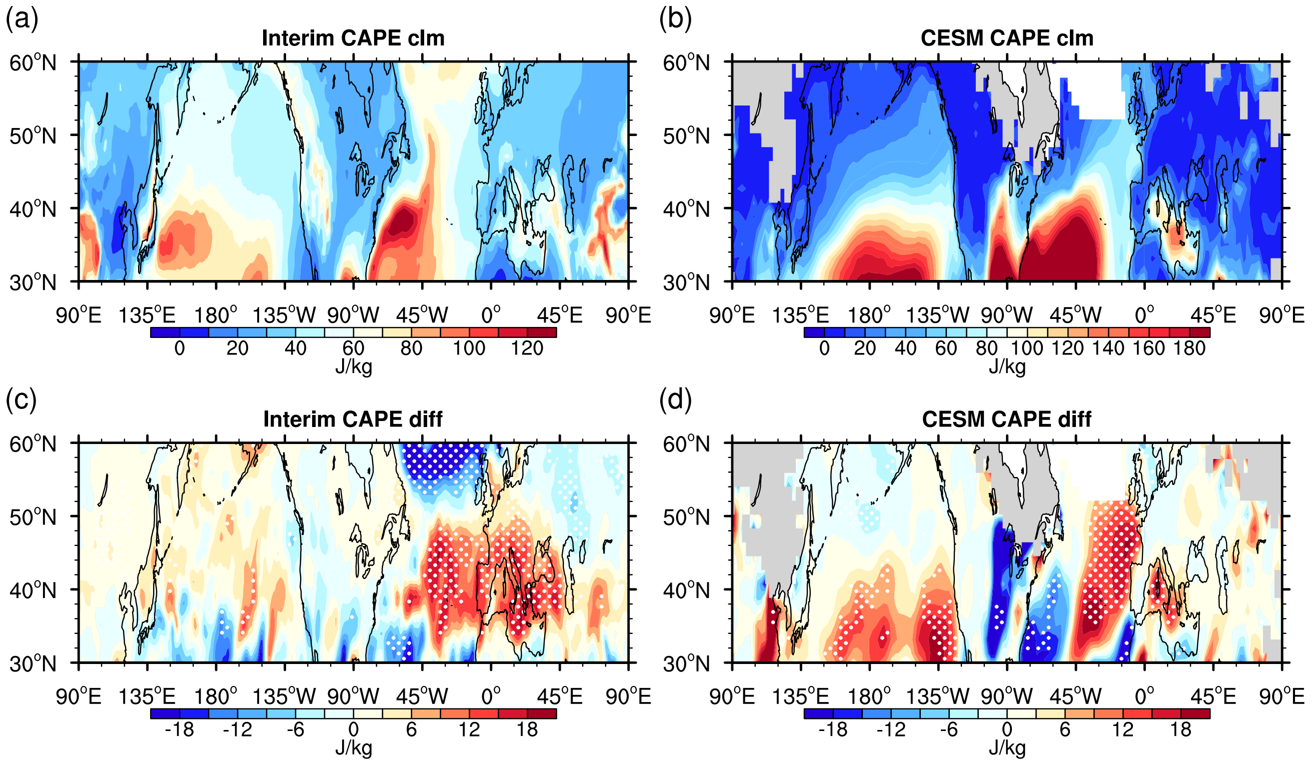

Fig. 8 (**a**) Climatological mean of CAPE (unit: J/kg) for the period 1980–2017 and (**c**) differences in CAPE (unit: J/kg) between weak and strong SPV events based on the ERA-Interim reanalysis data. (**b**) Climatological mean of CAPE (unit: J/kg) from R1 and (**d**) differences in CAPE (unit: J/kg) between R1 and R2. The differences over the dotted regions in (**c**) and (**d**) are statistically significant at the 90% confidence level according to the bootstrap test

30 and 60°N. Correspondingly, temperature decrease in the upper troposphere between 30 and 45°N is more significant than that in the lower troposphere (Fig. 10c and d). As a result, the tropospheric static ability to the south of 45°N is smaller during weak SPV events than during strong SPV events (Fig. 11), leading to a more unstable atmosphere and larger CAPE in the subtropical zones (Fig. 8c and d).

6 Conclusions and discussion

Based on the GPCP precipitation observations and ERA-Interim reanalysis data, the impacts of changes in the SPV strength on wintertime precipitation over the Northern Hemisphere are analyzed. The CESM climate model is also used to verify the statistical results. The CESM model can basically capture the main features of precipitation shown in the GPCP observations (Fig. 2). Overall, the anomalies of wintertime precipitation over the oceans are larger than those over the continents. The precipitation rates over the southeastern North Pacific and southern part of North Atlantic, and Southern Europe are larger during weak SPV events than during strong SPV events, whereas the total precipitation rates over the central North Pacific, the northern part of North Atlantic and Northern Europe become smaller during weak SPV events. An interesting feature is that the response of precipitation over the North Atlantic is stronger than that over the North Pacific. The spatial pattern of total precipitation changes over the North Pacific associated with SPV changes resembles that of large-scale precipitation changes, while significant convective precipitation changes mainly occur in southern part of North Pacific. By contrast, both the changes in large-scale and convective precipitation rates have important contributions to the total precipitation rate change over the North Atlantic (Fig. 3). Overall, the convective (large-scale) precipitation changes play a major role in the total precipitation changes over the southern (northern) parts of middle latitudes (Table 1).

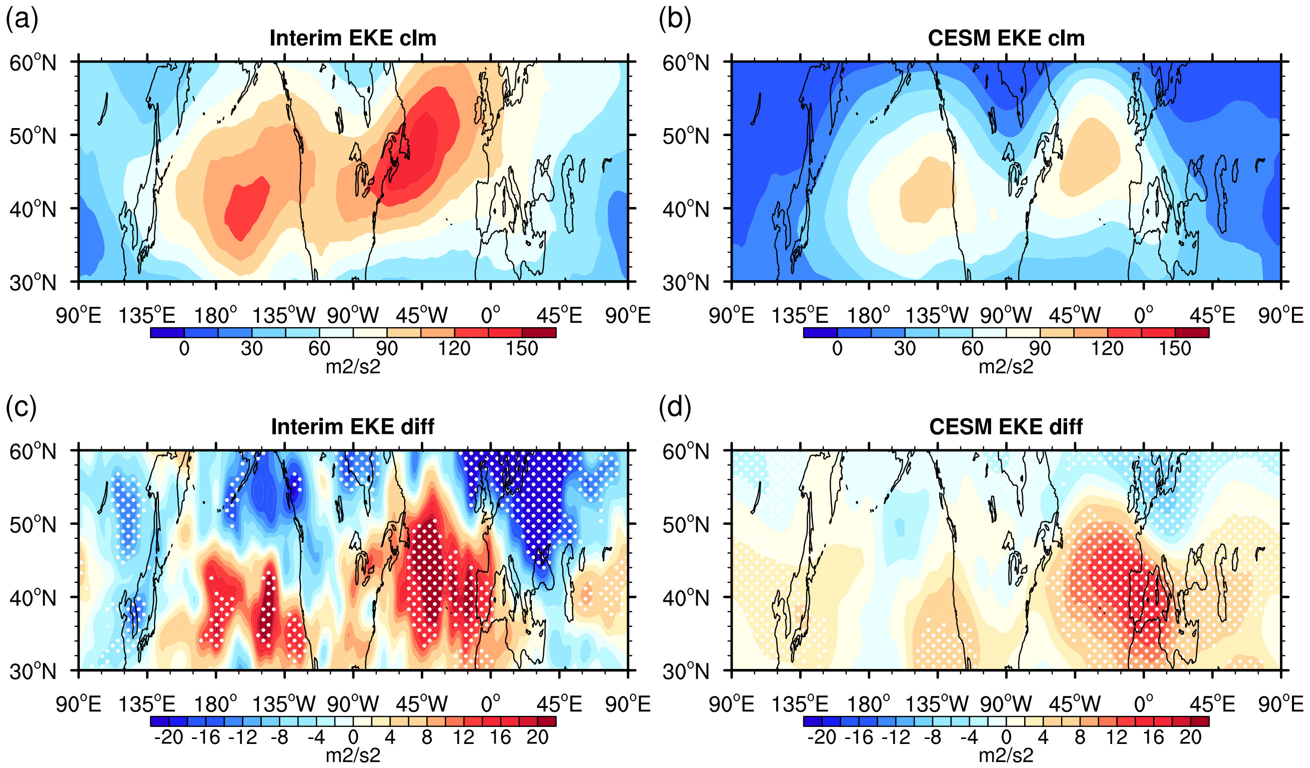

Fig. 9 (**a**) Climatological mean of 300 hPa EKE (unit: m^2/s^2) for the period 1980–2017 and (**c**) differences (unit: m^2/s^2) in 300 hPa EKE between weak and strong SPV events based on the ERA-Interim reanalysis data. (**b**) Climatological mean of 300 hPa EKE from R1 and (**d**) differences in 300 hPa EKE (unit: m^2/s^2) between R1 and R2. The differences over the dotted regions in (**c**) and (**d**) are statistically significant at the 90% confidence level according to the bootstrap test

Further analysis reveals the mechanisms responsible for precipitation changes induced by SPV changes over the North Pacific and North Atlantic. The changes in large-scale precipitation are closely related to large-scale circulation changes caused by stratosphere-troposphere coupling during anomalous SPV events. As the SPV weakens, the tropospheric zonal winds around 60°N decelerate. According to geostrophic equilibrium, negative geopotential height differences are located to the south of the weakened polar jet. As a result, there are anomalous cyclonic flows over the North Pacific and the North Atlantic during weak SPV events. The anomalous southerlies in the east of the cyclonic flows lead to larger convergence of water vapor flux and more large-scale precipitation in the southeastern North Pacific and Atlantic Oceans during weak SPV events. In contrast, the anomalous northerlies in the west of the cyclonic flows cause less precipitation over the central North Pacific and the western Atlantic Ocean.

The precipitation changes associated with SPV changes are larger over the North Atlantic than over the North Pacific, which is attributed to the stronger stratosphere-troposphere coupling over the former region. This is because there are stronger and barotropic wave-mean flow interactions over the North Atlantic Ocean (Figs. 6 and 7), which is consistent with previous studies (e.g. Breiteig 2008; Newman and Sardeshmukh 2008; Garfinkel et al. 2013). The wave feedback process over the North Atlantic is stronger than that over the North Pacific due to differences in the configuration of tropospheric jet core between the two oceans (Garfinkel et al. 2013). In the North Atlantic, there is a branch of jet stream in the tropospheric between 40 and 50°N where Rossby wave breaking is noticeable (Fig. 7c, d), while there is no such a branch of tropospheric jet stream, and wave

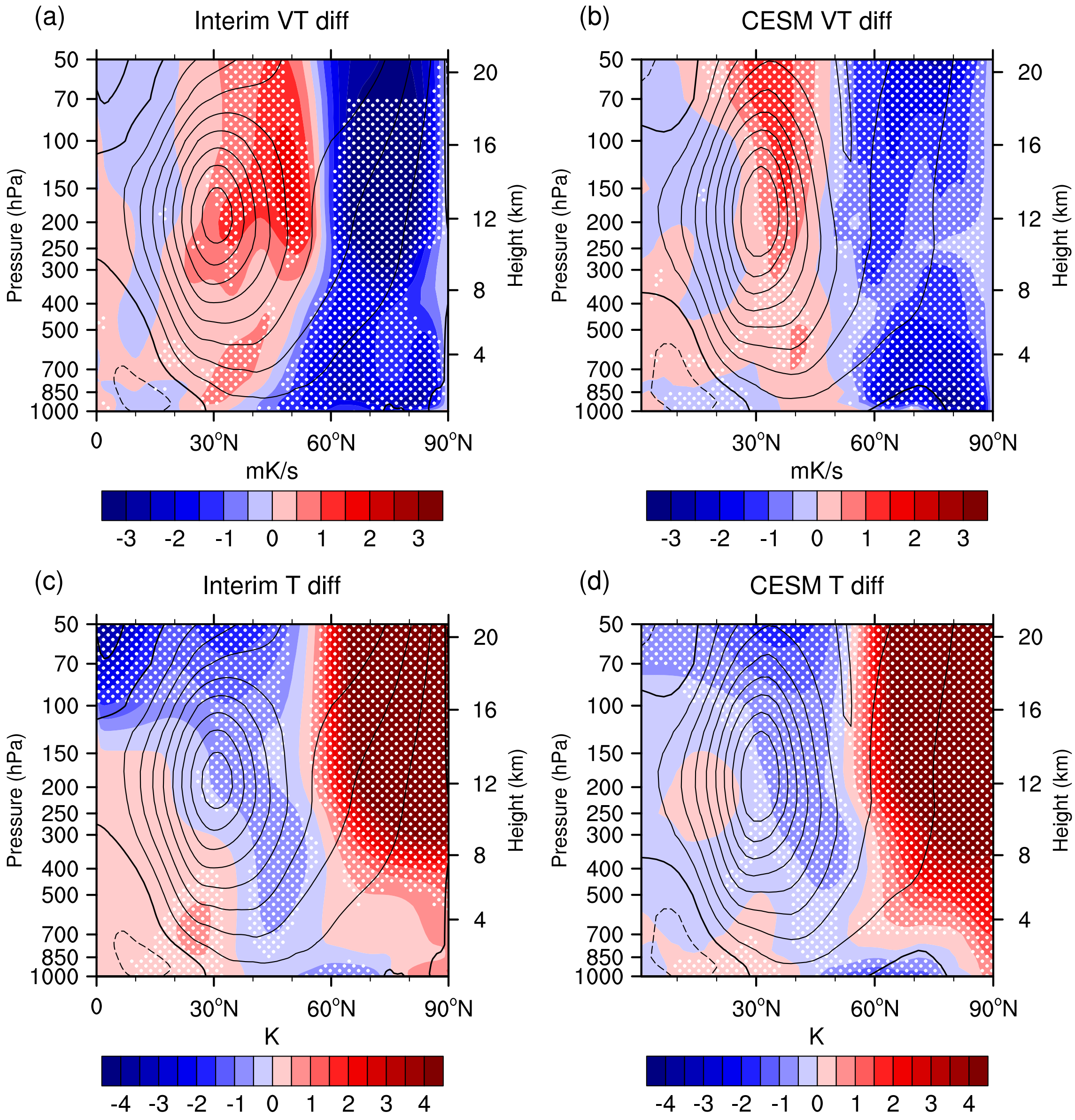

Fig. 10 Pressure-latitude cross sections of differences in zonal mean (**a**) eddy heat flux (unit: m K/s) and (**c**) temperature (unit: K) between weak and strong SPV events (color shaded) and climatological mean of zonal mean zonal winds (contours, unit: m/s, contour interval: 5 m/s, solid and dashed lines represent positive and negative values, respectively) for the period 1980–2017 based on the ERA-Interim reanalysis data. (**b**) and (**d**) are the same as (**a**) and (**c**), respectively, but for the differences between CESM R1 and R2 and climatological mean from R1. The differences over the dotted regions are statistically significant at the 90% confidence level according to the bootstrap test

flux convergence is weak in the troposphere at high latitudes over the North Pacific (Fig. 7a, b). Furthermore, the different stratosphere-troposphere coupling may be also related to ocean–atmosphere interaction mechanisms over the two oceans (e.g. Fang and Yang 2016; Guo and Tan 2018; Chen et al. 2020; Hu et al. 2021), which needs more research in the future.

There is more convective precipitation over the southern parts of the North Pacific and Atlantic Oceans during weak SPV events (Fig. 3d), which are caused by enhanced CAPE in the southern parts of the oceans. The more unstable atmosphere above these regions is related to larger heat transport by baroclinic waves from lower latitudes to higher latitudes (Fig. 10), which leads to reduced temperature and static ability in the subtropical middle and upper troposphere. In fact, all these features are consistent with the equatorward shifts of the subtropical jet stream and the baroclinic zone (Fig. 6 and Fig. 9).

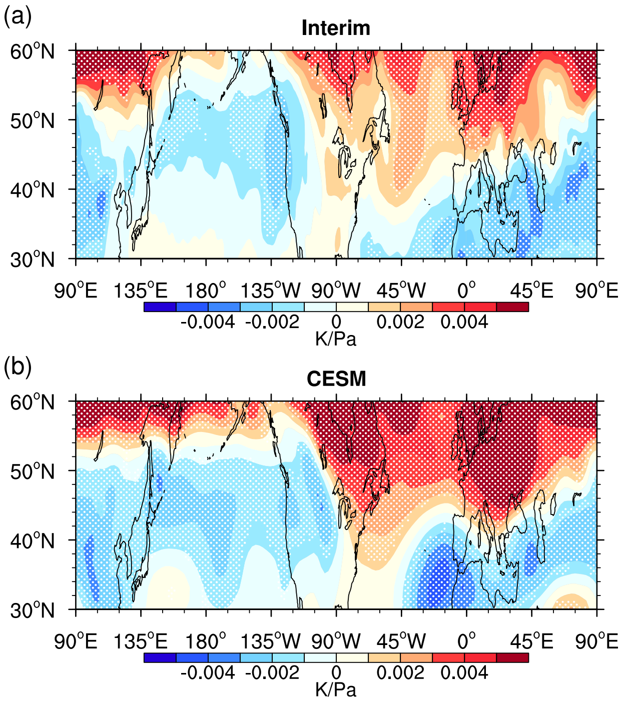

Fig. 11 (**a**) Differences in static ability averaged from 1000 to 200 hPa (unit: K/Pa) between weak and strong SPV events based on the ERA-Interim reanalysis data. (**b**) is the same as (**a**), but for the differences between R1 and R2. The differences over the dotted regions are statistically significant at the 90% confidence level according to the bootstrap test

Acknowledgements This research is supported by Project supported by Southern Marine Science and Engineering Guangdong Laboratory (Zhuhai) (No. SML2021SP312) and the National Natural Science Foundation of China (42075062, 42130601). This research is also supported by the Fundamental Research Funds for the Central Universities (lzujbky-2021-ey04) and Young Doctoral Funds for Gansu Provincial Education Department (2021QB-009). We thank ECWMF and NOAA for providing data. We are grateful that NCAR provides CESM model. We also appreciate the computing support provided by Supercomputing Center of Lanzhou University.

References

Adler R, Huffman G, Chang A et al (2003) The version2 global precipitation climatology project (GPCP) monthly precipitation analysis (1979–present). J Hydrometeorol. https://doi.org/10.1175/15257541(2003)004%3c1147:TVGPCP%3e2.0.CO;2

Ambaum MHP, Hoskins BJ (2002) The NAO troposphere–stratosphere connection. J Clim 15:1969–1978. https://doi.org/10.1175/15200442(2002)015%3c1969:TNTSC%3e2.0.CO;2

Bai K, Chang N-B, Gao W (2016) Quantification of relative contribution of Antarctic ozone depletion to increased austral extratropical precipitation during 1979–2013. J Geophys Res 121:1459–1474. https://doi.org/10.1002/2015JD024247

Baldwin M, Dunkerton T (2001) Stratospheric harbingers of anomalous weather regimes. Science 294:581–584. https://doi.org/10.1126/science.1063315

Blackmon ML (1976) A climatological spectral study of the 500 mb geopotential height of the northern hemisphere. J Atmos Sci 33:1607–1623

Boljka L, Birner T (2020) Tropopause-level planetary wave source and its role in two-way troposphere–stratosphere coupling. Weather Clim Dyn 1:555–575. https://doi.org/10.5194/wcd-1-555-2020

Breiteig T (2008) Extra-tropical synoptic cyclones and downward propagating anomalies in the Northern Annular mode. Geophys Res Lett. https://doi.org/10.1029/2007GL032972

Charlton-Perez AJ, Huang WTK, Lee SH (2021) Impact of sudden stratospheric warmings on United Kingdom mortality. Atmos Sci Lett 22:e1013. https://doi.org/10.1002/asl.1013

Chen Q, Li Z, Fan G et al (2011) Indications of stratospheric anomalies in the freezing rain and snow disaster in South China, 2008. Sci China Earth Sci 54:1248. https://doi.org/10.1007/s11430-011-4192-3

Chen L, Fang J, Yang X-Q (2020) Midlatitude unstable air-sea interaction with atmospheric transient eddy dynamical forcing in an analytical coupled model. Clim Dyn 55:2557–2577. https://doi.org/10.1007/s00382-020-05405-0

Cohen J, Barlow M, Kushner PJ, Saito K (2007) Stratosphere–troposphere coupling and links with Eurasian land surface variability. J Clim 20:5335–5343. https://doi.org/10.1175/2007JCLI1725.1

Darand M, Pazhoh F (2019) Vertically integrated moisture flux convergence over Iran. Clim Dyn 53:3561–3582. https://doi.org/10.1007/s00382-019-04726-z

Davini P, Cagnazzo C, Anstey JA (2014) A blocking view of the stratosphere-troposphere coupling. J Geophys Res 119:11100–11115. https://doi.org/10.1002/2014JD021703

Dee DP, Uppala SM, Simmons AJ et al (2011) The ERA-interim reanalysis: configuration and performance of the data assimilation system. Q J R Meteorol Soc 137:553–597. https://doi.org/10.1002/qj.828

Domeisen DIV, Butler AH (2020) Stratospheric drivers of extreme events at the Earth's surface. Commun Earth Environ 1:1–8. https://doi.org/10.1038/s43247020-00060-z

Doswell CA, Rasmussen EN (1994) The effect of neglecting the virtual temperature correction on CAPE calculations. Weather Forecast 9:625–629

Douville H (2009) Stratospheric polar vortex influence on northern hemisphere winter climate variability. Geophys Res Lett. https://doi.org/10.1029/2009GL039334

Fang J, Yang X-Q (2016) Structure and dynamics of decadal anomalies in the wintertime midlatitude North Pacific ocean–atmosphere system. Clim Dyn 47:1989–2007. https://doi.org/10.1007/s00382-015-2946-x

Garfinkel CI, Hartmann DL (2011) The influence of the Quasi-Biennial oscillation on the troposphere in winter in a hierarchy of models. Part I: simplified dry GCMs. J Atmos Sci 68:1273–1289. https://doi.org/10.1175/2011JAS3665.1

Garfinkel CI, Waugh DW, Gerber EP (2013) The effect of tropospheric jet latitude on coupling between the stratospheric polar vortex and the troposphere. J Clim 26:2077–2095. https://doi.org/10.1175/JCLI-D-12-00301.1

Gelaro R, McCarty W, Suárez MJ et al (2017) The modern-era retrospective analysis for research and applications, version 2 (MERRA-2). J Clim 30:5419–5454. https://doi.org/10.1175/JCLI-D-16-0758.1

Gilleland E (2020) Bootstrap methods for statistical inference. Part I: comparative forecast verification for continuous variables. J Atmos Ocean Technol 37:2117–2134. https://doi.org/10.1175/JTECH-D-20-0069.1

Graf H-F, Zanchettin D, Timmreck C, Bittner M (2014) Observational constraints on the tropospheric and near-surface winter signature of the northern hemisphere stratospheric polar vortex. Clim Dyn 43:3245–3266. https://doi.org/10.1007/s00382-014-2101-0

Guo YP, Tan ZM (2018) Westward migration of tropical cyclone rapid-intensification over the northwestern Pacific during short duration El Niño. Nat Commun 9:1507. https://doi.org/10.1038/s41467-018-03945-y

Hartley D, Villarin J, Black R et al (1998) A new perspective on the dynamical link between the stratosphere and troposphere. Nature 391:471–474. https://doi.org/10.1038/35112

Haynes PH, McIntyre ME, Shepherd TG, Marks CJ, Shine KP (1991) On the "downward control" of extratropical diabatic circulations by Eddy-induced mean zonal forces. J Atmos Sci 48(4):651–678

Holton JR, Mass C (1976) Stratospheric vacillation cycles. J Atmos Sci 33:2218–2225. https://doi.org/10.1175/1520-0469(1976)033%3c2218:SVC%3e2.0.CO;2

Hoskins BJ, Hodges KI (2002) New perspectives on the northern hemisphere winter storm tracks. J Atmos Sci 59:1041–1061. https://doi.org/10.1175/15200469(2002)059%3c1041:NPOTNH%3e2.0.CO;2

Hu D, Guan Z, Tian W, Ren R (2018) Recent strengthening of the stratospheric Arctic vortex response to warming in the central North Pacific. Nat Commun 9:1697. https://doi.org/10.1038/s41467-018-04138-3

Hu D, Guan Z, Tian W (2019) Signatures of the Arctic stratospheric ozone in northern Hadley circulation extent and subtropical precipitation. Geophys Res Lett 46:12340–12349. https://doi.org/10.1029/2019GL085292

Hu D, Guan Z, Liu M, Wang T (2021) Is the relationship between stratospheric Arctic vortex and Arctic oscillation steady? J Geophys Res 126:e2021JD035759. https://doi.org/10.1029/2021JD035759

Huntingford C, Marsh T, Scaife AA et al (2014) Potential influences on the United Kingdom's floods of winter 2013/14. Nat Clim Change 4:769–777. https://doi.org/10.1038/nclimate2314

Kang S, Polvani L, Fyfe J, Sigmond M (2011) Impact of polar ozone depletion on subtropical precipitation. Science 332:951–4. https://doi.org/10.1126/science.1202131

Kidston J, Scaife AA, Hardiman SC et al (2015) Stratospheric influence on tropospheric jet streams, storm tracks and surface weather. Nat Geosci 8:433–440. https://doi.org/10.1038/ngeo2424

Knight JR, Maidens A, Watson PAG et al (2017) Global meteorological influences on the record UK rainfall of winter 2013–14. Environ Res Lett 12:074001. https://doi.org/10.1088/1748-9326/aa693c

Kolstad EW, Breiteig T, Scaife AA (2010) The association between stratospheric weak polar vortex events and cold air outbreaks in the northern hemisphere. Q J R Meteorol Soc 136:886–893. https://doi.org/10.1002/qj.620

Kretschmer M, Cohen J, Matthias V et al (2018) The different stratospheric influence on cold-extremes in Eurasia and north America. NPJ Clim Atmos Sci 1:1–10. https://doi.org/10.1038/s41612-018-0054-4

Kunz T, Fraedrich K, Lunkeit F (2009) Response of idealized baroclinic wave life cycles to stratospheric flow conditions. J Atmos Sci 66:2288–2302. https://doi.org/10.1175/2009JAS2827.1

Kushner PJ, Polvani LM (2004) Stratosphere–troposphere coupling in a relatively simple AGCM: the role of Eddies. J Clim 17:629–639

Li C, Wettstein JJ (2012) Thermally driven and Eddy-driven jet variability in reanalysis. J Clim 25:1587–1596. https://doi.org/10.1175/JCLI-D-11-00145.1

Li J, Fan K, Xu J et al (2017) The effect of preceding wintertime Arctic polar vortex on springtime NDVI patterns in boreal Eurasia, 1982–2015. Clim Dyn 49:23–35. https://doi.org/10.1007/s00382-016-3324-z

Lim E-P, Hendon HH, Arblaster JM et al (2016) Interaction of the recent 50 year SST trend and La Niña 2010: amplification of the southern annular mode and Australian springtime rainfall. Clim Dyn 47:2273–2291

Limpasuvan V, Hartmann DL (2000) Wave-maintained annular modes of climate variability. J Clim 13:4414–4429. https://doi.org/10.1175/15200442(2000)013%3c4414:WMAMOC%3e2.0.CO;2

Liu Y, Zhao Y, Guan Z (2008) Influences of stratospheric circulation anomalies on tropospheric weather of the heavy snowfall in January 2008. Clim Environ Res 13:548–555 (**in Chinese**)

Lubis SW, Huang CSY, Nakamura N et al (2018) Role of finite-amplitude rossby waves and nonconservative processes in downward migration of extratropical flow anomalies. J Atmos Sci 75:1385–1401. https://doi.org/10.1175/JAS-D-170376.1

Ma X, Xie F, Li J et al (2019) Effects of Arctic stratospheric ozone changes on spring precipitation in the northwestern United States. Atmos Chem Phys 19:861–875. https://doi.org/10.5194/acp-19-861-2019

Mbengue C, Schneider T (2017) Storm-track shifts under climate change: toward a mechanistic understanding using baroclinic mean available potential energy. J Atmos Sci 74:93–110. https://doi.org/10.1175/JAS-D-15-0267.1

Mitchell DM, Gray LJ, Anstey J et al (2013) The influence of stratospheric vortex displacements and splits on surface climate. J Clim 26:2668–2682. https://doi.org/10.1175/JCLI-D-12-00030.1

Newman M, Sardeshmukh PD (2008) Tropical and stratospheric influences on extratropical short-term climate variability. J Clim 21:4326–4347. https://doi.org/10.1175/2008JCLI2118.1

Overland JE, Wang M (2016) Recent extreme arctic temperatures are due to a split polar vortex. J Clim 29:5609–5616. https://doi.org/10.1175/JCLI-D-16-0320.1

Perlwitz J, Harnik N (2003) Observational evidence of a stratospheric influence on the troposphere by planetary wave reflection. J Clim 16:3011–3026

Perlwitz J, Harnik N (2004) Downward coupling between the stratosphere and troposphere: the relative roles of wave and zonal mean processes. J Clim 17:4902–4909. https://doi.org/10.1175/JCLI-3247.1

Purich A, Son S-W (2012) Impact of Antarctic ozone depletion and recovery on southern hemisphere precipitation, evaporation, and extreme changes. J Clim 25:3145–3154. https://doi.org/10.1175/JCLI-D-11-00383.1

Sigmond M, Scinocca JF, Kharin VV, Shepherd TG (2013) Enhanced seasonal forecast skill following stratospheric sudden warmings. Nat Geosci 6:98–102. https://doi.org/10.1038/ngeo1698

Smith KL, Neely RR, Marsh DR, Polvani LM (2014) The specified chemistry whole atmosphere community climate model (SC-WACCM). J Adv Model Earth Syst 6:883–901. https://doi.org/10.1002/2014MS000346

Son S-W, Tandon NF, Polvani LM, Waugh DW (2009) Ozone hole and southern hemisphere climate change. Geophys Res Lett. https://doi.org/10.1029/2009GL038671

Song Y, Robinson W (2004) Dynamical mechanisms for stratospheric influences on the troposphere. J Atmos Sci 61:1711–1725

Song L, Wu R (2019) Precursory signals of East Asian winter cold anomalies in stratospheric planetary wave pattern. Clim Dyn 52:5965–5983. https://doi.org/10.1007/s00382-018-4491-x

Tomassini L, Gerber EP, Baldwin MP et al (2012) The role of stratosphere-troposphere coupling in the occurrence of extreme winter cold spells over northern Europe. J Adv Model Earth Syst. https://doi.org/10.1029/2012MS000177

Vial J, Osborn TJ, Lott F (2013) Sudden stratospheric warmings and tropospheric blockings in a multi-century simulation of the

IPSL-CM5A coupled climate model. Clim Dyn 40:2401–2414. https://doi.org/10.1007/s00382-013-1675-2

Waugh DW, Sobel AH, Polvani LM (2017) What is the polar vortex and how does it influence weather? Bull Am Meteorol Soc 98:37–44

Wei K, Chen W, Huang R (2007) Dynamical diagnosis of the breakup of the stratospheric polar vortex in the northern hemisphere. Sci China Earth Sci 50:1369–1379. https://doi.org/10.1007/s11430-007-0100-2

Xie F, Li J, Tian W et al (2016) A connection from Arctic stratospheric ozone to El Niño-southern oscillation. Environ Res Lett 11:124026

Zhang GJ, McFarlane NA (1995) Sensitivity of climate simulations to the parameterization of cumulus convection in the Canadian climate centre general circulation model. Atmos Ocean 33:407–446. https://doi.org/10.1080/07055900.1995.9649539

Zhang M, Lin W, Bretherton CS et al (2003) A modified formulation of fractional stratiform condensation rate in the NCAR community atmospheric model (CAM2). J Geophys Res 108:4035. https://doi.org/10.1029/2002JD002523

Zhang J, Tian W, Chipperfield MP et al (2016) Persistent shift of the Arctic polar vortex towards the Eurasian continent in recent decades. Nat Clim Change 6:1094–1099. https://doi.org/10.1038/nclimate3136

Zhang K, Wang T, Xu M, Zhang J (2019) Influence of wintertime polar vortex variation on the climate over the north pacific during late winter and spring. Atmosphere 10:670. https://doi.org/10.3390/atmos10110670

Zhang R, Tian W, Wang T (2020) Role of the quasi-biennial oscillation in the downward extension of stratospheric northern annular mode anomalies. Clim Dyn 55:595–612. https://doi.org/10.1007/s00382-020-05285-4